Moving Contact Line Instability on Soluble Fibers

Jinhong Yang and Quanzi Yuan*

This paper presents a new kind of instability when inserting a soluble fiber into liquid. After wetting and dissolving the fiber by the liquid, the moving contact line (MCL) spontaneously loses stability. Because the sculpted shape of the fiber looks like a Chinese pagoda, this instability is named as the pagoda instability (PI). The coupling of dissolution and wetting leads to other special phenomena, i.e., dissolving-induced jet flow, and optimizes the fiber shape, etc. A criterion of PI is proposed and the competition between the interfacial energy and chemical potential to deduce the MCL motion and PI is shown. A phase diagram is used to summarize the final shapes of the fibers. By conducting atomic force microscopy (AFM) measurements, it is found that fibers with optimized shapes have a low adhesion force. Using the optimized fiber can decrease the influence of the capillary force during AFM measurements in humid environments by 70%.

1. Introduction

The study of the behaviors and mechanisms of wetting on fibers is of critical importance in the fields of directional droplet transportation,[1,2] coating,[3] the surface modification of fibers,[4] the preparation of micro-/nano-devices,[5] etc.

As we know, the wetting system develops in the direction of interfacial energy reduction or stays the same without external energy input. Besides, wetting should be treated as an irreversible process because it is the process of energy dissipation.[6] The instability of wetting on insoluble fibers requires the input of external energy. For example, a hydrophilic fiber touches the surface of water, the solid–air (SA) interface is replaced by the solid–water (SW) interface because of capillary rise (the interfacial energy of SW is smaller than that of SA), and the area of SA interface decreases.[7] Even keeping the fiber away from the surface of the water, the SW interface does not disappear, and the liquid on the fiber shrinks and breaks to the droplet. The interfacial energy of the system reduces, eventually (This phenomenon is known as Plateau–Rayleigh instability,[8] PRI).

J. Yang, Q. Yuan
State Key Laboratory of Nonlinear Mechanics
Institute of Mechanics
Chinese Academy of Sciences
Beijing 100190, P. R. China
E-mail: yuanquanzi@lnm.imech.ac.cn
J. Yang, Q. Yuan
School of Engineering Science
University of Chinese Academy of Sciences
Beijing 100049, P. R. China

The ORCID identification number(s) for the author(s) of this article can be found under https://doi.org/10.1002/admi.202201248.

Gendelman et al. found and analyzed a very impressed and interesting phenomenon that when polymer solutions were deposited on vertical plates and dried with hot air, mesoscopically ordered self-assembled polymer films were obtained because of Marangoni instability.[9]

In this work, we report a new instability on the soluble fiber surface, which seems beyond the law of interfacial energy evolution for wetting. In the experiments, the liquid completely slides off the surface of the fiber, and the area of the SA interface is larger than that before entering the water (see **Figure 1**a). The sculpted shape from the fiber looks like a Chinese pagoda, does not agree with the previous studies.[10–13] Therefore, we designate this instability as the pagoda instability (PI). Based on the mechanics and thermodynamics modeling, we reveal that the PI is formed by the competition among surface tensions and chemical potential. Under the atomic force microscopy (AFM) test, we further demonstrate that the tip with a pagoda shape can reduce capillary adhesion greatly.

2. Results and Discussion

In our cases, the deformation of the solid induced by shear stresses can be ignored because of the slow flow velocity. The sizes of the material defects (the defects are mainly bubbles, and their sizes are on the order of microns) are far smaller than the radii of the solids, so we can ignore the influence of the defects on the pagoda structure. Besides, we also ignore the influence of solid vibration. The fiber always keeps vertical with the surface of the liquid, and the schematic of the experimental facility is shown in Figure S1 and Movie S1, Supporting information.
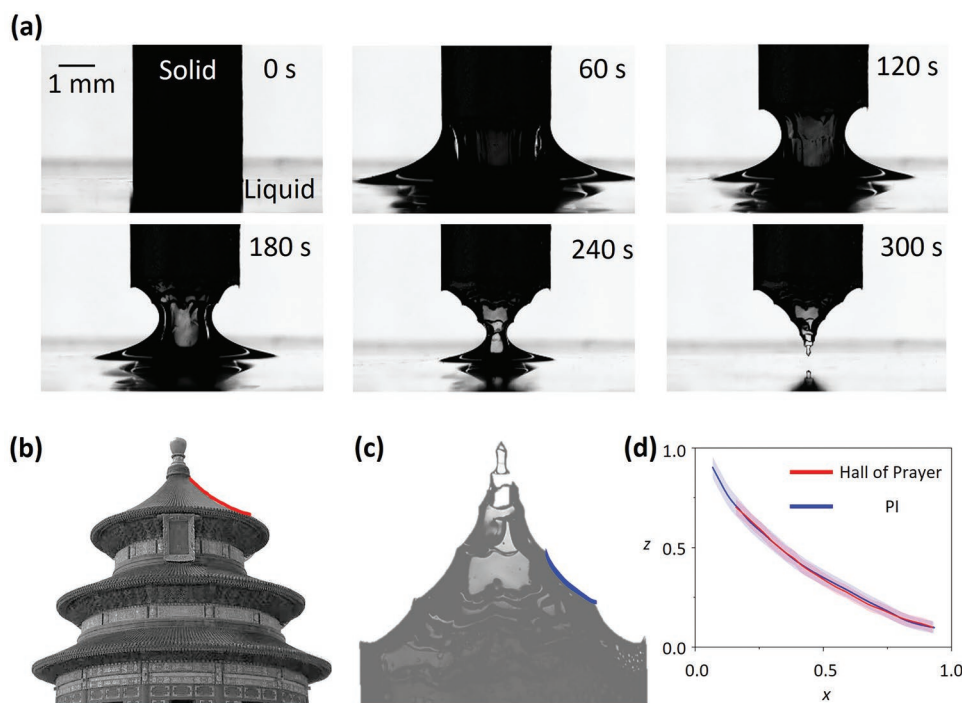
2.1. Characterization of PI

Inserting soluble fibers with different radii (0.5–5 mm) into the liquid induces PI and forms various structures. The water rises along the fiber wall to a certain height, and then the water–oil interface falls to a new position and rises again. This loop repeats until the liquid separates from the fiber (see Figure 1a). Every loop of the rise and fall is similar; thus, we propose that the forming process of the pagoda structure is self-similar. Therefore, after clarifying the forming mechanism for the first floor, we can deduce the whole process of fiber dissolving. The profile of the first floor is shown in **Figure 2**a. Without loss of

**ADVANCED
SCIENCE NEWS**
www.advancedsciencenews.com

**ADVANCED
MATERIALS
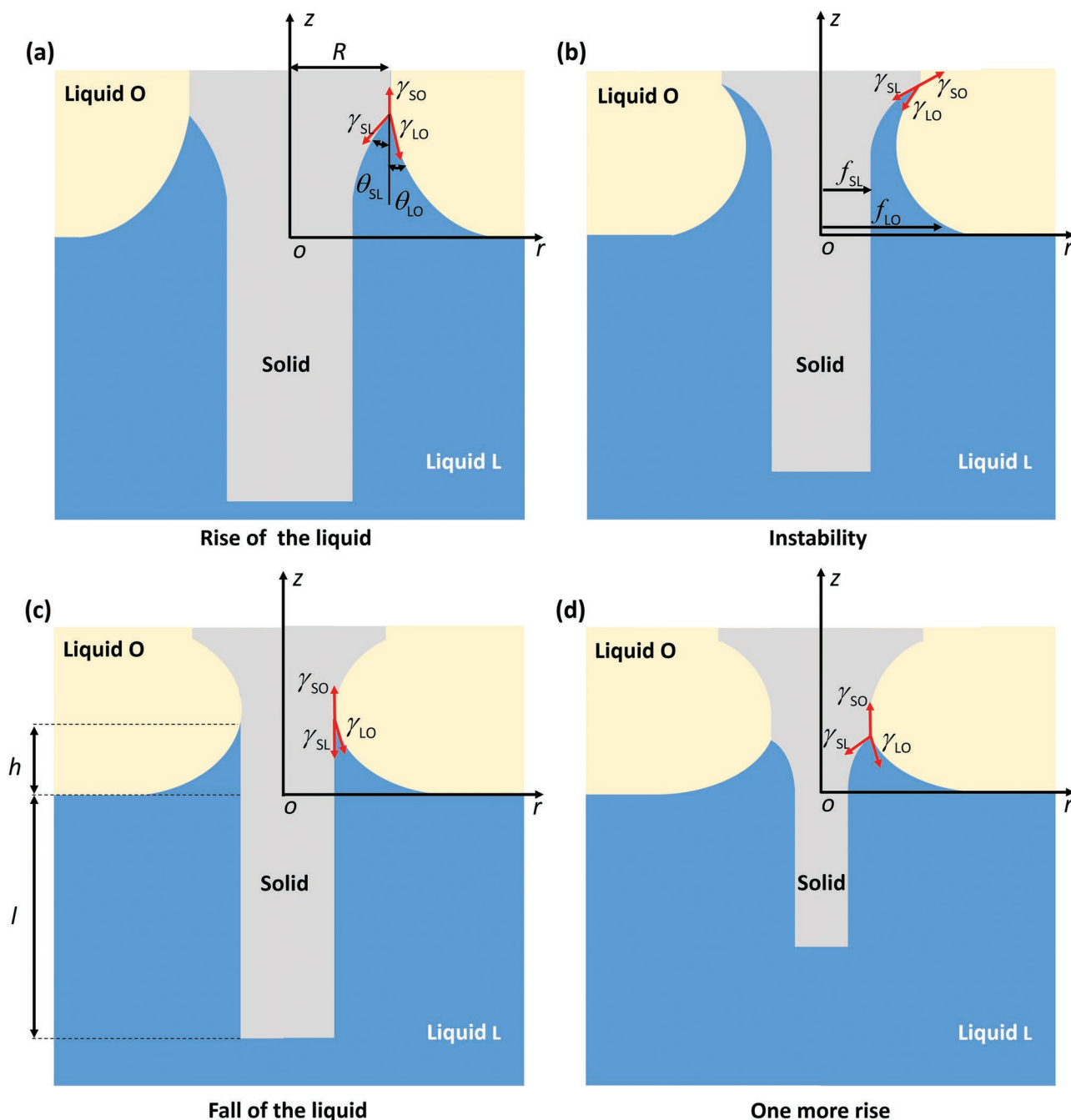INTERFACES**
www.advmatinterfaces.de

Figure 1. The process of pagoda instability. a) Time-lapse photography of the process of pagoda instability. b) Hall of Prayer for Good Harvests. c) A tip forming by PI. d) The shapes of the eaves and the tip.

generality, we build a model in which the fiber is surrounded by two liquids. One is a solvent (denoted by L), and the other is a covering that is immiscible with the solute and solvent (denoted by O). If the outside factors can be ignored, the covering does not need to be considered in the experiments. In this case, the symbol O represents air. The dissolution on the surface of the fiber results in instability, and the forming process of the pagoda structure can be divided into three stages: liquid rise, instability, and liquid fall.

2.2. Rise of Liquid on the Soluble Fiber

Unbalanced forces cause the liquid to rise. The dimensionless numbers involved in the study of wetting include the Capillary number Ca, Reynolds number Re, and Bond number Bo. In our experiments, the Capillary number $Ca = \eta_L v / \gamma_{LO}$ is much smaller than 1 (the viscosity of liquid L $\eta_L \approx 10^{-3}$ Pa s, the flow velocity near the liquid L–liquid O (LO) interface $v \approx 10^{-4}$ m s^{-1}, the surface tension $\gamma_{LO} \approx 10^{-2}$ N m^{-1}), so the surface tension is larger than viscosity force. The Reynolds number $Re = \rho_L v L / \eta_L \approx 10^{-2}$ (the density of liquid L $\rho_L \approx 10^3$ kg m^{-3}, the characteristic length $L \approx 10^{-4}$ m), so the viscosity force is larger than inertia force. The effect of inertia can be ignored. The Bond number $Bo = \rho_L g L^2 / \gamma_{LO} \approx 10^{-2}$ (the acceleration of gravity g is 10 m s^{-2}), so the surface tension is larger than gravity. We ignore the gravity effect on the LO interface based on the low Bond number. We analyze the driving forces and resistances that arise from free energy and dissipation, respectively. Free energy consists of interfacial energy and chemical potential resulting from dissolution and rise. With the change

in interface shape induced by dissolution and rise, the direction of surface tensions and the interfaces vary, and then the interface energies change. It is worth to noted that the influence of concentration on surface tensions is so slight that it can be ignored based on the results of experiments.[14] When the solute enters the liquid from the solid, solvent molecules surround it.[15] Therefore, the chemical potential is related to the construction of solute molecules apart from the concentration. We use the solvation energy density Γ, i.e., the chemical potential per unit volume of the solid, to characterize the solute influence on the solution.[16] The dissolution effect can be expressed as a force with surface tension dimension $\Gamma c_s \varepsilon$, where ε and c_s are the cutoff of the moving contact line (MCL)[17] and the saturation concentration of the solute, respectively. The dissipation is induced by contact line "friction" and liquid viscosity.[18] The contact friction can be expressed as $\pi \xi_{cl} R_n \dot{h}$, where ξ_{cl} is the friction parameter, R_n is the nth floor initial radius, and $\dot{h}$ is the liquid rise velocity. The viscosity dissipation mainly exists in the boundary layers of liquid L and liquid O. The viscosity related dissipation induced by the rise of liquid L is expressed as $3\pi \eta_L R_n \delta_L^{-1} \int_0^h v^2 \, dz$, where η and δ are the liquid viscosity and the boundary layer thickness, respectively. The subscript I notes as L or O, and they are liquid L or liquid O, respectively. Considering $v \sim \dot{h}$, the boundary layer thickness δ_I is proportional to $\sqrt{\eta_L R_n / \rho_L \dot{h}}$, where ρ is the density of the liquid. Because the rise velocity is slow, we hypothesize that the process of rise is quasi-static. In other words, the driving forces always maintain a balance with the resistance. Consequently, based on Onsager's variational principle[17] and ignoring the change in Capillary number (see Supporting Information S2), we obtain the scaling law of liquid rise:

**ADVANCED
SCIENCE NEWS**
www.advancedsciencenews.com

**ADVANCED
MATERIALS
INTERFACES**
www.advmatinterfaces.de

Figure 2. Schematics of the model. a) Liquid O rises along the soluble fiber, while liquid L dissolves the solid. When the liquid rises to a certain position H_n, the LO interface bends to the fiber. b) Contact line instability occurs. c) After the instability, liquid L falls to the new position. Finally, the liquid rises again and enters the next loop until the liquid separates from the fiber. d) The liquid rises again.

$$\frac{h}{R_n} = \left(\frac{t}{\tau}\right)^{1/3} \tag{1}$$

Here, $\tau = (C_\gamma - 2\xi_{cl})/(R_n^3 C_a^2)$ is the characteristic time, and C_γ and C_a are constants. Liquid rises with the advancing angle[19] θ_A, which is the sum of θ_{SL} and θ_{LO}. With increasing contact angle θ_{SL}, the contact angle θ_{LO} decreases, and the rise velocity of the liquid slows down.

2.3. Recession of the Solid–Liquid (SL) Interface

In our case, the solute is heavier than the solvent, so the high-concentration liquid flows along the direction of gravity. The diameter of the solid keeps decreasing until the liquid separating from the solid, and the diameter of the solid inside liquid L affects the final results. To avoid the evaporation and condensation of the liquid, in our experiment, the silicone oil (liquid O) is coved on the surface of water (liquid L). Therefore,
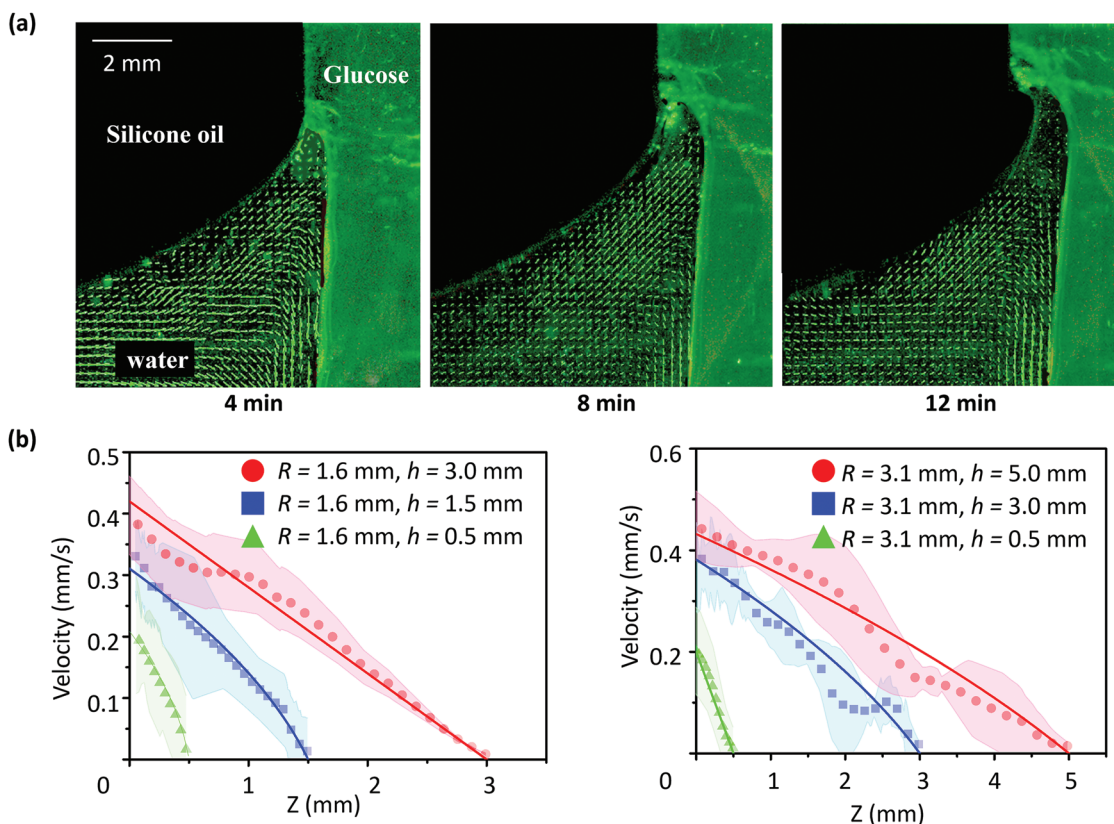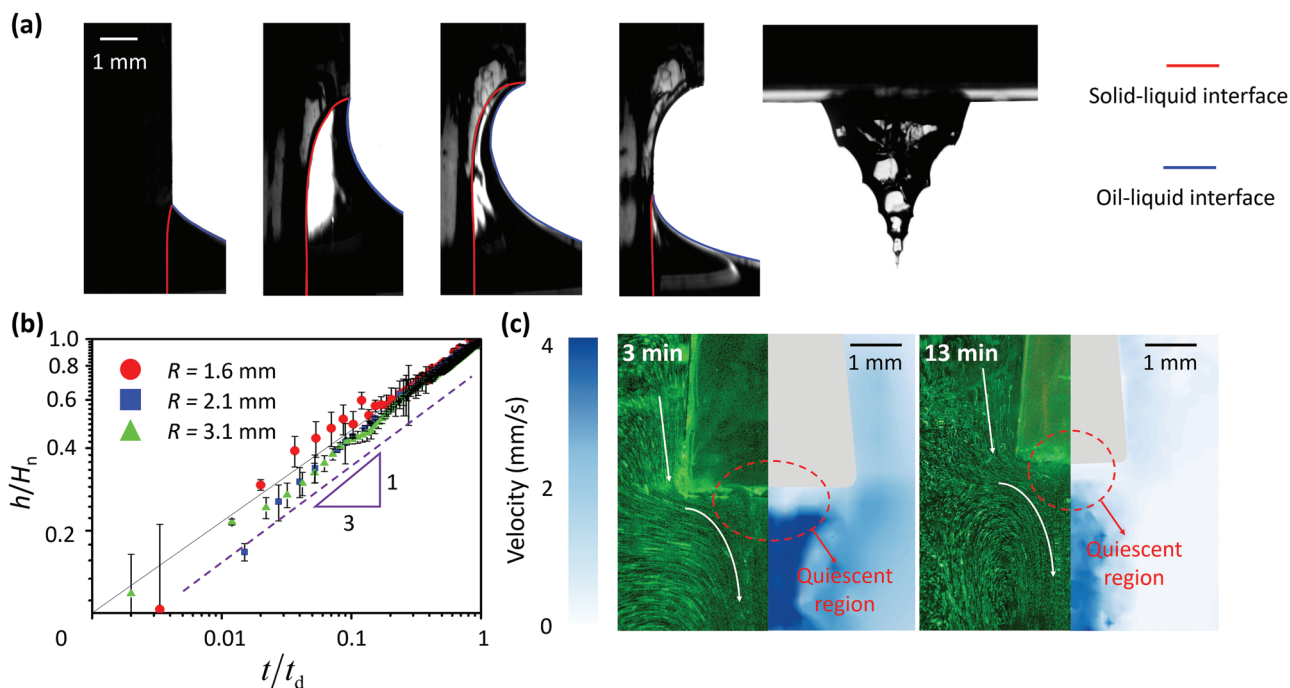
Figure 3. Flow field. a) The low-concentration liquid flows up along the water–silicone oil interface and dissolves the glucose. The high-concentration liquid containing glucose flows down while the SL interface recedes. b) Plots show the velocity distribution near the SL interface. The points (circle, square, triangle) are the raw data, the lines are the fitting curves.

solid only dissolves when it contacts with liquids. As shown in **Figure 3**b, dissolution takes place in the boundary layers near the SL interface and results in dissolving-induced jet flow. The thickness of the boundary layer depends on the viscosity η_L and diffusivity D. The relative importance of the viscosity and the diffusivity can be characterized by the Schmidt number $Sc = \eta_L/(\rho_L D)$, and we estimate $Sc \approx 10^3$ in most cases. Therefore, the large Schmidt number implies that the solid dissolves into the solvent by the shear effect rather than diffusion. Besides, for the sculpted processes dominated by diffusion, the final shape of the solid is similar to the initial shape of the solid. Obviously, the sculpted fibers in our case are much different from the initial shape. In our case, the dissolution velocity of the radial direction depends on the shear stress in the boundary layer $\overline{\delta}_{SL}$, i.e., $v_n \propto |\tau| \sim \eta_c v_g/\overline{\delta}_{SL}$,[20] where v_g and η_c are the flow velocity and characteristic viscosity of liquid in the boundary layer $\overline{\delta}_{SL}$, respectively. Here, the boundary layer thickness near the SL interface is $\overline{\delta}_{SL} \propto \sqrt{\eta_c R_n/(\rho_c U_N)}$, where ρ_c is the characteristic density of liquid in this boundary layer, and U_N is the characteristic flow velocity near the SL interface. The buoyancy differences in fluid induce near-body flows and develop the interface layer.[13] Therefore, the characteristic flow velocity near the SL interface $U_N = \sqrt{\beta g c_s R_n}$,[21] where g and β are the gravitational acceleration, and the solutal expansion coefficient, respectively. The velocity is fitted by raw data and expressed as $v_g = U_N(1-z/h)^{1/2}$ (see Figure 3). As we said before, the SL interface recedes with the rise of liquid. Thus, the dissolution time

is dominated by liquid rise; then, we can obtain the dissolution time as $t_d \propto (h^3 - z^3)$, according to Equation (1). Obviously, the profile of the SL interface can be represented as $f_{SL} = v_n t_d$. We assume that the dissolution of solid below the horizon ($z < 0$) is uniform because the slope of the fiber wall is small ($<5°$). Therefore, we believe that the shape from the fiber below the horizon remains cylindrical; thus, the dissolution time and dissolution velocity satisfy $t_d \propto h^3$ and $v_n|_{z=0}$, respectively. It is worth explaining that the dissolution in the zone below the horizon is different because the flow separation occurs at the end of fiber. There is a quiescent region on the bottom of the fiber because the flow separates from the end of the fiber. In the quiescent region, the flow velocity is very slow and $\approx 10^{-8}$ m s^{-1}. The transport method of the solute depends on the relative importance of the flow velocity and diffusion velocity, the ratio of which is the Péclet number. As we mentioned before, the diffusivity D is $\approx 10^{-9}$ m^2 s^{-1}, and the size of the quiescent region δ_q is $\approx 10^{-4}$ m by experimental measurements. The Péclet number is 10^{-2} and so low that the convection effect can be ignored in the quiescent region. The change in the fiber length can be expressed as $\Delta l = D(c_s - \overline{c})t_d/\delta_q$. In addition, the profile of the LO interface satisfies the equation $f_{LO}/\sqrt{1+(df_{LO}/dz)^2} = R_n$. The condition $df_{LO}/dz|_{z=h} = \tan\theta_{SL}$ leads to the function of the LO interface, i.e.

$$f_{LO} = \frac{R_n}{2}\left[(1-\tan(\theta_{LO}))e^{-(H_n-z)/R_n} + (1+\tan(\theta_{LO}))e^{(H_n-z)/R_n}\right] - R_n \quad (2)$$

**ADVANCED
SCIENCE NEWS**

www.advancedsciencenews.com

**ADVANCED
MATERIALS
INTERFACES**

www.advmatinterfaces.de

Figure 4. Interface evolution of a dissolving fiber. a) Time-lapse photos showing the change at the interface. Red lines and blue lines are the SL and LO interfaces, which are obtained by theory. b) Plot showing the change in height h with time. t_d is the time necessary to rise. c) PIV experiment indicating that the quiescent region exists at the bottom of the fiber.

where $\theta_{LO} = \theta_A - \theta_{SL}$, the advancing angle of liquid L moving on the solid is obtained by experimental measurements. The θ_{SL} can be obtained by the slope of function f_{SL} at MCL, i.e., $\theta_{SL} = \arctan\left(df_{SL}/dz\big|_{z=h}\right)$. According to **Figure 4**, the key to pagoda construction formation is liquid fall caused by instability. Therefore, we further studied the process of MCL instability.

2.4. Criterion of PI

According to the results of the experiments (**Figure 5**), the instability differs from PRI. From an energy perspective, liquid rise is a process of free energy desecration. For the rise without dissolution, the SL interface replaces the SO interface, having a lower interfacial energy. During the rise of liquid on the surface of the soluble fiber, liquid rise accompanies dissolution. The SL interface replaces the SO interface, while solute molecules enter the solvent, further reducing the free energy. As a result, the height of the liquid rise accompanied by dissolution is higher than that without dissolution. According to the above analyses, we built a model to calculate the change in the free energy F, which is a function of the liquid height h and includes the change in interfacial energy and chemical potential of the solution, i.e., $F = \gamma_{SL}\Delta A_{SL} + \gamma_{SO}\Delta A_{SO} + \gamma_{LO}\Delta A_{LO} + \int\Gamma c\,dV_{SL}$, where ΔA is the change of the area. Here, the change in free energy in different stages is calculated by the numerical method and shown in Figure 5a. Obviously, with the rise of liquid along the fiber, the free energy has the minimum value, i.e., a potential well. Elaborating on this process, the free energy decreases because the area of the SL interface increases, resulting from the rise and dissolution of the liquid. The dissolution continues

to proceed because the solution is unsaturated. The perturbation makes the liquid oscillate around the potential well $(dF/dh = 0, \quad d^2F/dh^2 > 0)$. We further calculate the changes in free energy during liquid fall (the formula of free energy is shown in Supporting Information S3), the results of which are shown in Figure 5a by the blue lines. Free energy decreases with the fall of liquid. Given that the position of the potential well is not the stable point of the system, the MCL losses are stable in the position of the potential well. Figure 5 shows that the liquid does not fall to the origin and stops at a certain position, which we call the recovery of stability unless the liquid separates from the fiber during sliding. It is noted that the liquid falls with the receding angle, which distinguishes it from the advancing angle. In the process of liquid fall, the fall velocity is much higher than the dissolution velocity; thus, we disregard the dissolution during liquid fall. As liquid L dissolves the solid, the LO interface loses stability as soon as liquid L reaches a certain height H_n, which is the height of the nth floor. For getting the criterion of the instability, we study the change of the free energy before and after instability (see Supporting Information S4). The perturbation of the height for the MCL results in the change of the free energy δF, and it can be expressed as $\delta F = -\gamma_{SO}\delta A_{SO} + \gamma_{SW}\delta A_{SW} + \gamma_{WO}\delta A_{SO} + \Delta\bar{c}\delta V_{SO}$, where V denotes as the volume. When $\delta F < 0$, the system is stable and the MCL remains rising. When $\delta F > 0$, the system is unstable, and the liquid falls. According to the critical state $\delta F = 0$, we can obtain the criterion of the instability:

$$\frac{H_n^4}{R^{5/2}} \propto \frac{\gamma_{SO} - \gamma_{SW} - \gamma_{WO}}{\Gamma} \tag{3}$$
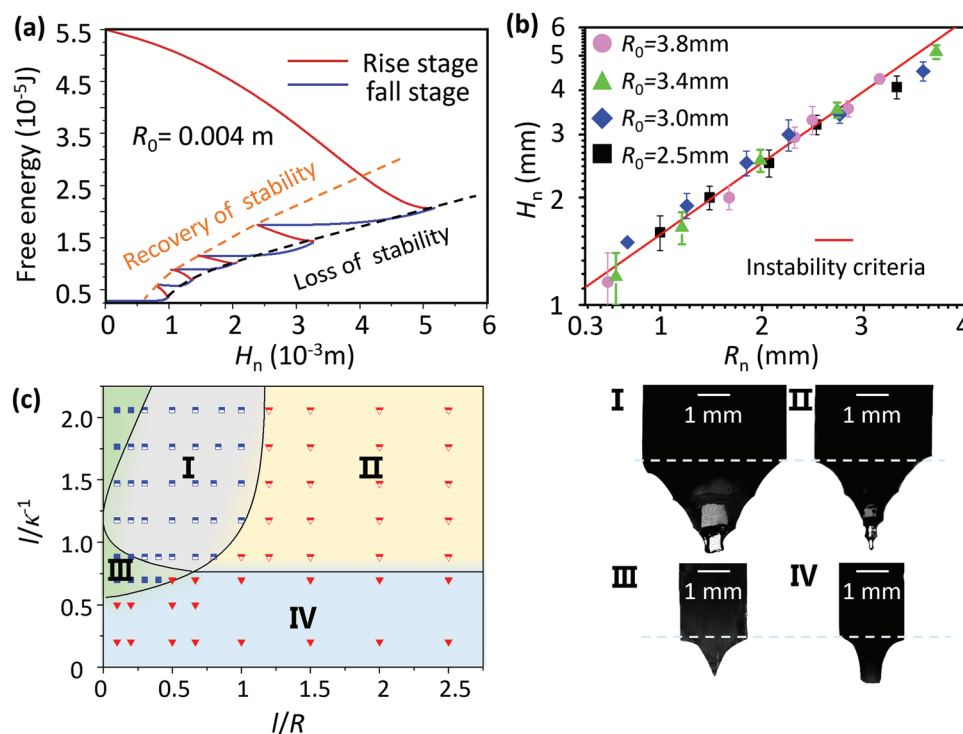
Figure 5. Criterion of pagoda instability and shapes from dissolving fibers. a) The diagram of the free energy shows that the change in energy in every loop (one rise and one fall) is similar. b) The instability criterion, showing that the change in the scaling law of H_n with R_n is 5/8. c) Diagram showing the geometrical conditions for obtaining different shapes of fibers, which include pagoda-like with a flat end, pagoda-like with a cuspidal tip, single floor with a cuspidal tip, and single floor with a flat end.

Consequently, the criterion can be expressed as $H_n \propto R_n^{5/8}$. PI is also the result of the competition between chemical potential and interfacial energy.

We disregard the dissolution effect during liquid fall because the falling velocity is much faster than the dissolution velocity. Therefore, the height of stability recovery can be expressed as

$$J_n \propto R_{n-1} \ln \frac{2\kappa^{-1}}{R_{n-1}} \tag{4}$$

which is similar to the height of the meniscus on the insoluble surface. The curves in **Figure 6**a also show that the PI is periodic, which is the reason why the solvent erodes the fiber into pagoda structures. According to Figure 5a, the variations in free energy in each instability are similar, which further proves that fiber erosion is a self-similarity process.

2.5. Formation of Fiber for Different Shape

In Figure 5c, we summarize the experimental results of the different radii (0.5–5 mm) of the fiber. It is worth to noted that it is difficult to control the experimental conditions (the environment vibration, solid deformation, material defects, water entry angle of solids, and so on) of the fiber with small radius (<0.5 mm), so we do not discuss the results of the fiber with a small radius. We mention that the fiber can be eroded into different shapes, including a single floor, a pagoda-like structure, a cuspidal tip, and a flat end. Here, we elaborate on the

formation of the tip. During the formation of the tip, the dissolution velocity on the fiber wall (radial direction) competes with that at the bottom of the fiber (axial direction). As we mentioned before, the convection effect dominates the dissolution
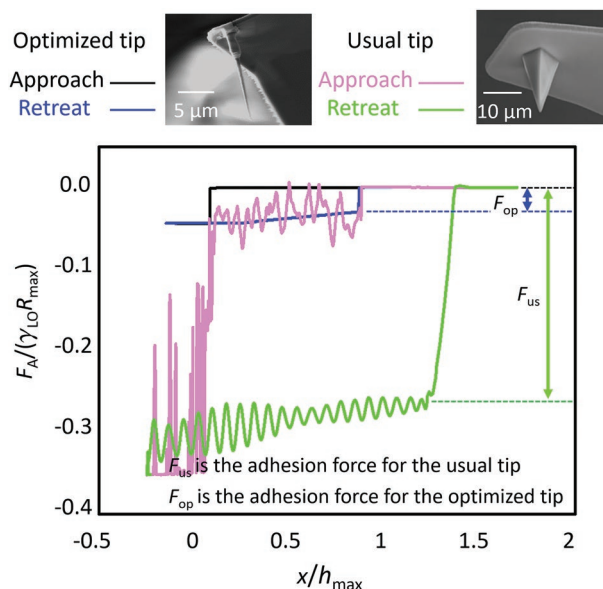
Figure 6. Measuring adhesion force by AFM. The black and pink lines are the loading curves of the optimized tip and usual tip (Bruker MLCT), respectively. The blue and green lines are the unloading curves of the optimized tip and usual tip, respectively.

on the fiber wall, and the diffusion effect dominates the dissolution at the bottom of the fiber. Thus, in general, the dissolution velocity in the axial direction is slower than that in the radial direction. Unless the insertion depth of the fiber inserted is small, the fiber becomes a cuspidal tip. When the liquid separates from the fiber or the dissolution depth in the radial direction is greater than the radius of the fiber during the first instability, the fiber will form a single floor. Because of the axial dissolution of the fiber, the inserted depth l is the key parameter that decides the shape of the tip. According to the parameters l and R_0, we divide fibers into four types in the phase diagram (Figure 5c). When the solid is merely in contact with the Liquid L, i.e., $l = 0$, the fiber with large radius (0.5–5 mm) will be dissolved into single floor with a flat end (type IV). However, we do not discuss the results of the fibers with the microscopic or mesoscopic diameters, because it is difficult to produce the specimens and control the positions of specimens to merely contact with the liquid L.

2.6. Adhesion Force of the Reshaped Fiber

We use AFM to measure the adhesion force of the reshaped fiber on air–liquid interface by contact mode, and the results of the AFM experiment are shown in Figure 6. The adhesion force on the surface of the fiber is about 10 nN and much smaller than that of the common commercial probe (Bruker MLCT). The special shape of the tip helps to prevent the adhesion of liquid and can be found in some substances with low surface energy, such as pollen[22] and spiky particles.[23]

3. Conclusion

In summary, we observe and explain the dynamic process of inserting a soluble fiber into liquid. The liquid rises along the soluble fiber to a certain height, which is proportional to the initial radius to the power of 5/8, and then the MCL loses stability and falls. The competition between the interfacial energy and chemical potential induces the movement and instability of the MCL. In some cases, the liquid repeats the process of rise and fall until it separates from the fiber completely. Because every instability is self-similar, the fiber forms a pagoda structure. We further demonstrate that the PI-optimized fiber has low-adhesion characteristics can be a general strategy for low-adhesion design, such as hydrophobic surface,[24] micro-needle patches for the rapid and painless injection of drugs,[25] fabrication of AFM probe,[26] heat exchange devices based on the spontaneous dewetting,[27] and so on.

4. Experimental Section

Sample Preparation: Glucose was melted at 250 °C and became caramel. The liquid of caramel was poured into a mold made by polydimethylsiloxane. The caramel from the mold was removed when the caramel cooled. The radii of the fiber were ranging from 0.5 to 5 mm. The fiber was fixed in the lifting platform to control the position of the fiber. Water was used as the solvent, and the size of the container used to hold the water was 205 × 145 × 200 mm. The fiber with a thin layer of silicone oil to prevent the influence of humidity on the experiment was covered. Images were captured from the side view by a camera.

Preparation of Particle Image Velocity (PIV) Experiment: PIV technology was used to observe and record the flow field. A sheet light with a 0.5 mm light waist was produced by a semiconductor laser (LASERWAVE LWGL532-5W-L). Polystyrene beads (Bangs Laboratories. Inc. PS07001) with a 6 µm radius were mixed with water. The flow of the beads was recorded by high-speed camera (Revealer M220) in 1000 fps.

Adhesion Force Measurement: In the AFM experiments, the optimized tip made of copper fiber was prepared by electrochemical corrosion. The initial diameter of the copper fiber was 100 µm. The electrolyte consisted of calcium chloride ($CaCl_2$), water (H_2O), and hydrochloric acid (HCl), and the volume ratio of the three was $CaCl_2 : H_2O : HCl = 60:36:4$. The voltage of electrochemical corrosion was 25 V. The final shape of the fiber was single floor with a cuspidal tip (the diameter of the tips was 50 nm). The copper fiber was cut with the optimized tip and it was glued with the AFM probe (Bruker NP-O10) without the tip by Focused Ion beam (FIB, Helios NanolabG3 CX). The adhesion test was conducted by AFM (Asylum MFP-3D infinity) in contact mode. The curve of the force versus the distance between the tip and the surface of the water was recorded. The water was fully filled in a container with 35 × 35 × 5 mm.

Supporting Information

Supporting Information is available from the Wiley Online Library or from the author.

Conflict of Interest

The authors declare no conflict of interest.

Data Availability Statement

The data that support the findings of this study are available from the corresponding author upon reasonable request.

[1] P. B. Bintein, H. Bense, C. Clanet, D. Quéré, *Nat. Phys.* **2019**, *15*, 1027.

[2] Y. Zheng, H. Bai, Z. Huang, X. Tian, F. Q. Nie, Y. Zhao, J. Zhai, L. Jiang, *Nature* **2010**, *463*, 640.

**ADVANCED
SCIENCE NEWS**

www.advancedsciencenews.com

**ADVANCED
MATERIALS
INTERFACES**

www.advmatinterfaces.de

[3] A. Charles-Orszag, F. C. Tsai, D. Bonazzi, V. Manriquez, M. Sachse, A. Mallet, A. Salles, K. Melican, R. Staneva, A. Bertin, C. Millien, S. Goussard, P. Lafaye, S. Shorte, M. Piel, J. Krijnse-Locker, F. Brochard-Wyart, P. Bassereau, G. Duménil, *Nat. Commun.* **2018**, *9*, 4450.

[4] J. J. Kaufman, G. Tao, S. Shabahang, E. H. Banaei, D. S. Deng, X. D. Liang, G. S. Johnson, Y. Fink, A. F. Abouraddy, *Nature* **2012**, *487*, 463.

[5] F. Panciera, M. M. Norton, S. B. Alam, S. Hofmann, K. Mølhave, F. M. Ross, *Nat. Commun.* **2016**, *7*, 11479.

[6] X. F. Yang, *Appl. Phys. Lett.* **1995**, *67*, 2249.

[7] P. G. De Gennes, F. Brochard-Wyart, D. Quéré, *Capillarity and Wetting Phenomena: Drops, Bubbles, Pearls, Waves*, Springer, New York, USA **2004**.

[8] S. Haefner, M. Benzaquen, O. Bäumchen, T. Salez, R. Peters, J. D. McGraw, K. Jacobs, E. Raphaël, K. Dalnoki-Veress, *Nat. Commun.* **2015**, *6*, 7409.

[9] E. Bormashenko, R. Pogreb, O. Stanevsky, Y. Bormashenko, T. Stein, V. Zeev Gaisin, R. Cohen, O. V. Gendelman, *Macromol. Mater. Eng.* **2005**, *290*, 114.

[10] L. Rayleigh, *Philos. Mag.* **1892**, *5*, 145.

[11] L. Rayleigh, *P. Lond. Math. Soc.* **1878**, *1*, 4.

[12] G. Wang, J. J. Lannutti, *Metall. Mater. Trans. A* **1995**, *26*, 1499.

[13] M. S. D. Wykes, J. M. Huang, G. A. Hajjar, L. Ristroph, *Phys. Rev. Fluids* **2018**, *3*, 043801.

[14] A. Docoslis, R. Giese, C. J. Van Oss, *Colloids Surf., B* **2000**, *19*, 147.

[15] Q. Z. Yuan, J. H. Yang, Y. Sui, Y. P. Zhao, *Langmuir* **2017**, *33*, 6464.

[16] J. H. Yang, Q. Z. Yuan, Y. P. Zhao, *Sci. China: Phys., Mech. Astron.* **2019**, *62*, 124611.

[17] P. G. De Gennes, *Rev. Mod. Phys.* **1985**, *57*, 827.

[18] X. K. Man, M. Doi, *Phys. Rev. Lett.* **2017**, *119*, 044502.

[19] T. J. Singler, S. Su, L. Yin, B. T. Murray, *J. Mater. Sci.* **2012**, *47*, 8261.

[20] M. N. Moore, L. Ristroph, S. Childress, J. Zhang, M. J. Shelley, *Phys. Fluids* **2013**, *25*, 116602.

[21] K. L. Chong, Y. S. Li, C. Ng, S. R. Verzicco, D. Lohse, *J. Fluid Mech.* **2020**, *892*, A21.

[22] S. Ito, S. N. Gorb, *ACS Appl. Mater. Interfaces* **2019**, *11*, 24691.

[23] H. J. Chen, T. Hang, C. D. Yang, G. S. Liu, D. A. Lin, J. M. Wu, S. L. Pan, B. R. Yang, J. Taoa, X. Xie, *Nanoscale* **2018**, *10*, 1978.

[24] C. S. Sharma, C. Stamatopoulos, R. Suter, P. R. von Rohr, D. Poulikakos, *ACS Appl. Mater. Interfaces* **2018**, *10*, 29127.

[25] J. Yu, Y. Zhang, Y. Ye, R. DiSanto, W. Sun, D. Ranson, Z. Gu, *Proc. Natl. Acad. Sci. U. S. A.* **2015**, *112*, 8260.

[26] H. Plank, R. Winkler, C. H. Schwalb, J. Hütner, J. D. Fowlkes, P. D. Rack, I. Utke, M. Huth, *Micromachines* **2019**, *11*, 48.

[27] C. W. Lo, Y. C. Chu, M. H. Yen, M. C. Lu, *Joule* **2019**, *3*, 2806.

2201248 (8 of 8)